nature portfolio

https://doi.org/10.1038/s41586-025-08987-z

Supplementary information

Radiative forcing reduced by early twenty-first century increase in land albedo

In the format provided by the authors and unedited

Radiative forcing reduced by early 21st century increase in land albedo

Zhengyang Hou[1], Liqiang Zhang[1,2*], Jingjing Peng[3], Giovanni Forzieri[4], Aolin Jia[5], Zhiqiang Xiao[1], Ying Qu[1], Jintai Lin[6,7*], Duoying Ji[1], Zidong Zhu[1], Xin Yao[1], Shuwen Peng[1], Lanpu Zhao[2], Wenjie Fan[8], Zhaocong Wu[2], Hao Geng[1], Qihao Wang[1], Chenghu Zhou[9*], Suhong Liu[1] and Liangpei Zhang[2*]

[1]State Key Laboratory of Remote Sensing and Digital Earth, Faculty of Geographical Science, Beijing Normal University, Beijing, China.

[2]Aerospace Information Research Institute, Henan Academy of Sciences, Zhengzhou, China.

[3]Earth System Science Interdisciplinary Center/ Cooperative Institute for Satellite Earth System Studies (CISESS), University of Maryland, College Park, MD, USA.

[4]Department of Civil and Environmental Engineering, University of Florence, Florence, Italy.

[5]Remote Sensing and Natural Resource Modeling, Department ERIN, Luxembourg Institute of Science and Technology, Belvaux, Luxembourg.

[6]Laboratory for Climate and Ocean–Atmosphere Studies, Department of Atmospheric and Oceanic Sciences, School of Physics, Peking University, Beijing, China.

[7]Institute of Carbon Neutrality, Peking University, Beijing, China.

[8]School of Earth and Space Sciences, Peking University, Beijing, China.

[9]State Key Laboratory of Resources and Environmental Information System, Institute of Geographical Science and Natural Resources, Chinese Academy of Sciences, Beijing, China.

The File Includes:

1 Supplementary Texts 1-7

2 Supplementary Figures 1-26

3 Supplementary Tables 1-6

1 Supplementary Texts

1.1 Supplementary Text 1

Four-dimensional inverse distance weighting (IDW) interpolation model. The IDW interpolation is a method used to estimate the value of a variable at unsampled locations based on the nearby known point values. The basic principle is that the closer a point is to the location of interest, the more influence it has on the interpolated value[1].

The four-dimensional IDW interpolation model combines with data anisotropies to reconstruct missing albedo values in the four ALLUMs. Specifically, in each of the four ALLUMs, land surface albedo values under the same LULC type t, spectral band b, and albedo type w (white-sky or black-sky) are structured into four-dimensional arrays $D^{\alpha}_{t,b,w}(y, m, lon, lat)$. There are N arrays, where $N = 6 \times N_t$ (3 spectral bands, 2 albedo types, and N_t is the number of LULC types in each of the ALLUM datasets). The four dimensions of the array represent year (y), month (m), longitude (lon) and latitude (lat), respectively. Over 70 million grid-level albedo pairs (α_{ga} and α_{gb}) extracted for two $1^{\circ}\times1^{\circ}$ grid cells ga and gb are randomly selected to regress the anisotropic weights of each $D^{\alpha}_{t,b,w}$ by using Eq. (1).

$$\begin{aligned} |\alpha_{ga} - \alpha_{gb}| = &(dw_y \cdot \Delta y_{ga-gb})^2 + (dw_m \cdot \Delta m_{ga-gb})^2 \\ &+ (dw_{lon} \cdot \Delta lon_{ga-gb})^2 + (dw_{lat} \cdot \Delta lat_{ga-gb})^2 \end{aligned} \tag{1}$$

where α_{ga} and α_{gb} are from the same $D^{\alpha}_{t,b,w}$. Δy_{ga-gb}, Δm_{ga-gb}, Δlon_{ga-gb} and Δlat_{ga-gb} represent the distances between ga and gb along the four dimensions, respectively. dw_y, dw_m, dw_{lon}, and dw_{lat} represent the anisotropic distance weights. The weights account for the gradients of errors, which increase with distances between interpolation grid cells and neighboring grid cells.

Such metrics are then used to estimate the distance d_{gm-gn} from the missing grid gm to each of its neighboring grids gn as follows:

$$\begin{aligned} distance_{gm-gn} = &[(dw_y \cdot \Delta y_{gm-gn})^2 + (dw_m \cdot \Delta m_{gm-gn})^2 \\ &+ (dw_{lon} \cdot \Delta lon_{gm-gn})^2 + (dw_{lat} \cdot \Delta lat_{gm-gn})^2]^{\frac{1}{2}} \end{aligned} \tag{2}$$

Missing albedo values are then estimated as the weighted average of the nearest 20 pixels without missing values, by using the inverse distance $\left(1/distance_{ga-gb}\right)^2$ as weights.

1.2 Supplementary Text 2

Significance and fluctuations of albedo and induced changes in radiative forcing due to snow dynamics. The albedo changes in the global snow-free regions showed a significant increasing trend (Mann–Kendall test; P-value=0.0478; the gray line in Fig.1a in the main text; see Student's t-test and Mann-Kendall test in local snow-free albedo changes in Extended Data Fig. 2a and b in the main text) largely driven by the long-term changes in surface properties such as vegetation and water. Albedo changes in snow-free region were usually less than 0.1 over the past two decades, whereas areas that became snow-covered often experienced an increase in albedo by 0.5 or more. Our results indicate that the interannual fluctuations of snow cover affected the statistical significance of albedo trends both at grid cell and global level. Based on the Mann-Kendall test(P-value < 0.05), the regions with statistically significant albedo trends account for 31.0% of the global land surface (Fig. 1b in the main text, with 23.8% showing an increase and 7.2% showing a decrease); and in snow-free regions, 38.1% of the considered domain exhibits statistically significant changes (Extended Data Fig. 2b in the main text, with 29.1% showing an increase and 8.4% showing a decrease). We further conduct significance tests by using the two-sided Student's t-test for albedo changes between two periods (2011-2020 and 2001-2010), the proportions of the regions with significant albedo changes for all land surfaces and snow-free regions are 26.8% (Fig. 1c in the main text, with 19.2% showing an increase and 7.7% showing a decrease) and 32.9% (Extended Data Fig. 2a in the main text in the main text; with 24.1% showing an increase and 8.9% showing a decrease), respectively.

During the period 2001-2020, the global total snow cover area exhibited a significant decreasing trend (Fig.1a in the main text; Mann–Kendall test; P-value = 0.009), and the year 2020 was not an anomalous year for snow cover (the linear regression residual was less than 1.5 times of the standard deviation). Furthermore, the global land surface mean albedo increase caused by the albedo change in snow-free regions was 2.5 times as large as the global land surface mean albedo decrease caused by snow dynamics during 2001-2020. These results indicate that the 20-year global land surface mean albedo changes exhibited a general trend in global land surface albedo over the past two decades, instead of being mainly explained as the fluctuations caused by snow cover change.

In high-latitude regions, the extensive snow-covered areas received very weak shortwave radiation, which reduced the radiative forcing effect associated with the changes in albedo. As a result, the albedo-induced radiative forcing due to global snow dynamics was only -13.5% of the radiative forcing caused by albedo increases in snow-free regions (Fig. 2a, d and Fig. 4b in the main text). Although snow dynamics introduced greater interannual fluctuations to global mean radiative forcing, they did not diminish the significance of the trend. Both the radiative forcing induced by albedo in global land and in global snow-free land showed a significant trend (Mann–Kendall test; P-value=0.0478 and

0.0010; the purple line and gray line in Fig. 2a in the main text; see Student's t-test and Mann-Kendall test in local radiative forcing changes in Extended Data Fig. 2a and b in the main text).

1.3 Supplementary Text 3

Reliability verification based on comparison with albedo data from multiple sources. To verify the reliability of our albedo results, we use the GLASS02B03 V50 albedo dataset [2] to calculate the global land surface mean albedo change. This GLASS02B03 V50 dataset, based on AVHRR and MODIS satellite instruments, provides black-sky and white-sky albedo retrievals at 8-day interval and 0.05° spatial resolution for the period from 1981 to 2022. We utilize the albedo data from 2001 to 2020 to synthesize blue-sky albedo using Eq. (8) in the main text, compute the annual mean albedo in the land areas where the solar zenith angle is less than 70°, and analyze the albedo changes. The global land surface mean albedo change calculated from GLASS02B03 V50 is 0.0009 per decade, slightly higher than the 0.0007 per decade obtained from ALLUMs (Extended Data Fig. 3a in the main text). The correlation in interannual variation reaches 0.96. The global spatial distributions of calculated absolute albedo changes and albedo trends from 2001 to 2020 by using the GLASS02B03 V50 and ALLUMs datasets exhibit a strong overall consistency (Extended Data Fig. 3b-e in the main text), thus corroborating the reliability of our findings.

We evaluate the albedo changes over Greenland and the Antarctic ice sheets, which are regions of particular interest, using ALLUMs, GLASS02B03 V50 albedo data [2], MOD10A1 C6.1 snow albedo [3], and the in-situ albedo observations [4] from automatic weather stations (AWSs) of the Greenland Climate Network (GC-Net) and the Programme for Monitoring of the Greenland Ice Sheet (PROMICE), respectively. The MOD10A1 daily snow albedo dataset, using a snow bidirectional reflectance model, is highly suitable for describing the optical properties of pixels predominantly covered by snow and ice [5]. Its reliability has been confirmed in prior studies [6, 7]. As shown in Figs. S6-S7, snow albedo trends derived from MOD10A1 C6.1 closely align with trends from ALLUMs in Greenland and Antarctic ice sheets, both for annual mean snow albedo and summer trends (June–August for Greenland [8]; and December, January, and February [9]). To ensure the consistency in the study area during the synthesis of the annual mean snow albedo, MOD10A1 C6.1 snow albedo dataset excludes the data in the regions with a solar zenith angle greater than 70°. Note that the ALLUMs snow albedo changes in most inland snow accumulation regions are below the calibration limit (0.7% per decade as the relative bias; see details in Supplementary Text 4) and are masked as gray regions in panels (c) and (f) in Figs. S6-S7; the albedo trends in these regions are considered uncertain.

Furthermore, we compare the ground-based albedo measurements from AWS stations with MCD43A3 C6.1 data; note that the ALLUMs data are derived from MCD43A3 C6.1. We collect the monthly albedo observation data from a total of 38 PROMICE and GC-Net AWS stations established before 2021. Despite some discrepancies due to spatial scale differences (21m radius for AWS vs. 500m pixels for MCD43A3 [10]), albedo observations from these AWS stations show strong consistencies with MCD43A3 blue-sky albedo (Fig.

S8a, R^2=0.86 and RMSE=0.07), which are also consistent with the results from Ye et al [11]. (R^2=0.88 and RMSE=0.06). Among the 38 stations, 12 stations, all from GC-Net, were established before 2001 and had relatively complete albedo observation records from 2001 to 2020. We calculate the long-term albedo change trends for these 12 GC-Net stations to validate the albedo trends derived from MCD43A3 data. Although the consistency between these stations and MCD43A3 albedo data is lower than that of other 26 stations established after 2001 (Figs. S8b and S8c, R^2=0.69 vs 0.84), the long-term trends are directionally consistent for most stations (Fig. S9). One exception is at the NASA-E station, which displayed an opposing trend for reasons not clear at the moment. Note that for the comparison between AMS and MCD43A3 C6.1, we only use data from May to August, as the data in other months have more than 15% missing values at all AWS stations and more than 20% missing values at the 12 stations established before 2001.

Discrepancies are observed in Greenland and Antarctic ice sheets between the albedo changes derived from GLASS02B03 V50 and our results. Figs. S10-S11 show Albedo change trend from the GLASS02B03 V50, MCD43A3 C6.1, and ALLUMs datasets in Greenland and Antarctic ice sheets, respectively. In Greenland, the albedo change from GLASS is lower than those of MCD43A3 and ALLUMs, with most of regions showing a declining trend (Fig. S10a and e). However, the MCD43A3 data demonstrates a stronger consistency with GC-Net observational data compared to the GLASS dataset (Fig. S10e and f). This is also supported by previous results reported in Ye et al. [11], the comparison between AWS albedo and MCD43A3 shows R^2 = 0.88, RMSE=0.06, and bias=-0.03, whereas the comparison with GLASS shows R^2=0.80, RMSE=0.13, and bias=-0.10. In some areas of Antarctic ice sheet, GLASS presents a larger albedo increase compared to other datasets (Fig. S11). However, in most areas of the Antarctic ice sheet, albedo changes are smaller than the calibration limit, and they are taken as uncertain. These areas are shown as gray regions in Fig. S11d and h, as well as Fig. S15. In contrast, the results in the unmasked regions exhibit a high consistency across all datasets.

Overall, the global land surface mean albedo change calculated from ALLUMs is largely consistent in temporal and spatial patterns with those derived from the GLASS02B03 V50 albedo product. Discrepancies between ALLUMs and GLASS2B3 are primarily observed in the polar ice- and snow-covered regions. Furthermore, our ALLUMs results show high consistencies with the albedo changes computed from MOD10A1 C6.1 snow albedo data and long-term AWS albedo observations from PROMICE and GC-NET. We mark the regions where the albedo change trends are below the calibration limit and highlight that these regions are subject to uncertainty. Most of the regions with discrepancies between ALLUMs and GLASS occur in Greenland and Antarctic ice sheet (Fig. S15). Robustness experiments demonstrate that uncertainties in albedo changes in these regions have minimal impacts on the global land surface mean albedo change (Supplementary Text 4, S13-S14, and Extended Data Fig. 4 in the main text).

1.4 Supplementary Text 4

Effects of the calibration errors of MODIS sensors. Calibration of the MODIS solar reflective bands primarily relies on the solar diffuser and the solar diffuser stability monitor. Due to instrument aging, the on-board calibrators alone are insufficient to accurately characterize the instrument's response at all scan angles [12, 13]. The Collection 6 (C6) MODIS land and atmosphere datasets were released in 2014, featuring significant revisions to the calibration approach to account for sensor aging [14]. A change in the response versus scan (RVS) calibration approach that used fixed desert sites was implemented in C6 for Terra MODIS since the beginning of the Terra mission on 24 Feb 2000 and for Aqua MODIS since 27 July 2016 [15, 16]. The calibration approach of C6 was applied to bands 8 and 9 of Aqua MODIS and to several bands of Terra MODIS. On July 9, 2017, this approach was extended to bands 1-4 of the Aqua sensor and used for reprocessing for the whole time series to obtain MODIS C6.1 [16].

To further build confidence on the calibration error of MCD43A3 C6.1 albedo data, we derive the long-term trends of monthly blue-sky albedo trends at the six pseudo-invariant calibration sites (PICSs) from 2001 to 2020 and use these trends as the calibration error for each site (Fig. S13). These six PICSs (Libya 1 and 4, Algeria 3 and 5, Mauritannia 1 and 2) have been recognized by the CEOS WGCV IVOS (Committee on Earth Observation Satellites/Working Group on Calibration & Validation/Infrared and Visible Optical Sensors) for calibration or validation of satellite data. For each PICS, each albedo value represents the average of pixels within a typical spatial extent (20 km radius) around that the PICS to reduce the variability of surface optical properties [17]. The blue-sky albedo is calculated using Eq. (8) in the main text. Our results indicate that the average trend across these six PICSs is 0.09% per decade, or 2.3×10^{-4} per decade of absolutely albedo trend corresponding to a global mean albedo of 0.25. This calibration error for the MCD43A3 C6.1 albedo is smaller than the 20-year global snow-free land surface mean albedo change (2.2%, or 0.0038, with a significant trend of 0.0011 per decade) and the overall global land surface mean albedo change (0.72%, or 0.0018, with no significant trend) by one order of magnitude.

To further assess the robustness of our albedo trend results, we establish a calibration limit based on the mean trend bias observed at the above six PICSs. We conservatively set the calibration limit at 0.7% per decade, based on the largest blue-sky albedo trend (0.66% per decade from Mauritania 2) among the six PICSs, even though the trend deviations at all other desert points are below 0.35% per decade. After that, we mask out all albedo changes below the calibration limit over all LULC conversion pathways or non-conversion regions of each grid cell in the four ALLUM datasets, and then recalculate the global land and snow-free land surface mean albedo changes. As shown in Extended Data Fig. 4 in the main text, the difference in the global land surface mean albedo change before and after the mask in the four ALLUMs is applied is less than 2×10^{-4}, while the difference in snow-free regions is less than 8×10^{-5}.

238 These very small differences indicate that our calculated albedo change are
239 little affected by the calibration error.

1.5 Supplementary Text 5

Comparisons with previous results on radiaitve forcing. Compared with previous research on albedo-induced radiative forcing caused by anthropogenic changes in land use [18–21], our findings exhibit agreements.

Land-use forcing is defined as those changes in land-surface properties directly resulting from human activity rather than by climate processes (IPCC AR6). Lejeune et al. [21] and Smith et al. [20] individually quantified land-use radiative forcing using CMIP5 and CMIP6 models. Their results were -0.11±0.09 W/m^2 during 1850-2014 and -0.11 (-0.16 to -0.04) W/m^2 during 1850-2000. The two studies focus on the differences in radiative forcing driven by land use change which mainly shifts in agricultural practices and deforestation, leading to transitions between primary and secondary lands. Ghimire et al. [19] provided a MODIS/AVHRR-based estimate of radiative forcing value at approximately -0.12 W/m^2 from 1850, consistent with CMIP5 and CMIP6 outputs. They establish a mapping approach between the 6 land-use types in Land-use Harmonization (LUH) dataset [22] and the 17 land cover types defined by the International Geosphere-Biosphere Plan (IGBP), and reconstruct LULC conversions at 500m spatial resolution. Radiative forcing is calculated by integrating the reconstructed LULC conversions with an albedo lookup map devoid of interannual variations [23]. Building on these results, the IPCC AR6 estimated land-use radiative forcing at -0.15±0.1 W/m^2 for 1750-2019, excluding 0.05 W/m^2 from irrigation. On a per-decade basis, the radiative forcing is -0.0056 W/m^2/decade on average.

We adopt Ghimire's mapping methodology to classify the IGBP's 15 land cover types (excluding permanent snow and water bodies) into 6 LULC types of the LUH dataset (Supplementary Table S6). The conversions between the 6 land-use types from 2001 to 2020 result in negative radiative forcing of -0.0101 [-0.0119, -0.0081] W/m^2, or -0.0053 [-0.0063, -0.0043] W/m^2/decade, consistent with 0.0056 W/m^2/decade given in the IPCC AR6.

1.6 Supplementary Text 6

Limitations of our approach and potential impacts. Firstly, since the ALLUMs data are at the monthly scale, they are unable to capture higher-frequency (i.e. day-to-day) changes, such as those in snow/ice albedo caused by changes in algae.

Secondly, we synthesize the blue-sky albedo and ignore the anisotropic scattering of diffuse skylight, which may result in an albedo bias of 0.004-0.013 in snow-covered regions[24]. However, this has a very small impact on our findings. Since we focus on detecting albedo changes in global snow-free land regions, the influence of anisotropic scattering of diffuse skylight on blue-sky retrieval is minimal. Moreover, snow albedo is much higher than that of other land cover types, and albedo changes in regions transitioning between snow-covered and snow-free conditions often exceed 0.3 absolute units, meaning that an albedo bias of 0.013 absolute units reduced by the full expression method would have little effects on this change. For albedo-induced radiative forcing resulting from snow dynamics, there are significant uncertainties, as demonstrated by the variation in radiative forcing values calculated from the six radiative kernels (ranging from 0.0059 to 0.0277 W/m^2). These uncertainties far exceed the impact of the 0.013 absolute units of albedo bias reduced by the full expression method.

Finally, we calculate radiative forcing using albedo data that include the regions with solar zenith angles up to 70°-85°, as the calculation of global mean radiative forcing requires accounting for radiative flux changes across the entire land surface. The albedo data in these regions have significant uncertainties. Despite this, the impact on our results is minimal, as the estimation error of global mean radiative forcing due to the uncertainty in the high-albedo data from these regions is mitigated by the very low solar radiation flux. In the regions with solar zenith angles of 70°-85°, the average response in the top-of-atmosphere radiative flux to a given amount of surface albedo change (measured using the average of the six radiative kernels) is just 20.6% of the response in the regions with solar zenith angles less than 70°. Additionally, our results shows the actual albedo change in the regions with solar zenith angles of 70°-85° over 2001-2020 only contributes to 3.7% of the total albedo-induced global mean radiative forcing.

1.7 Supplementary Text 7

The global land surface mean albedo change and global mean radiative forcing induced by photosynthetic vegetation cover, non-photosynthetic vegetation cover and surface water content changes. In the main text, we have already explained how to calculate the contribution of these three components to the white/black-sky albedo changes for each month and 500m-resolution pixel $C^{Z}_{\alpha-pixel}(m,p,w)$, where m, p, and w represent the month, pixel, and albedo type (white-sky or black-sky), respectively. Z refers to $\ln NDVI$, SSI or $NMDI$, characterizing photosynthetic vegetation cover, non-photosynthetic vegetation cover and surface water content, respectively. The contribution of the three components to blue-sky albedo change in each pixel $C^{Z}_{\alpha-pixel}(m,p,blue)$ is calculated using Eq. (3), similar to Eq. (8) in the main text.

$$\begin{aligned} C^{Z}_{\alpha-pixel}(m,p,blue) =& C^{Z}_{\alpha-pixel}(m,p,white)\cdot DDRF \\ &+ C^{Z}_{\alpha-pixel}(m,p,black)\cdot(1-DDRF) \end{aligned} \tag{3}$$

where $DDRF$ is the fraction of diffuse downward radiation and, and is resampled to each 500m-resolution pixel. The method used to calculate $DDRF$ is described in Section 4.2 in the main text.

The global land surface mean albedo change induced by the three components is calculated by weighting and summing $C^{Z}_{\alpha-pixel}(m,p,blue)$ using Eq. (4).

$$\begin{aligned} &C^{Z}_{\alpha GL}(m,p,blue) = \frac{1}{A_{GL}}\cdot \\ &\sum_{pixel=1}^{N_{pixel}} \frac{\sum_{m=1}^{12} C^{Z}_{\alpha-pixel}(m,p,blue)\cdot A_{pixel}(p)\cdot M_{70}(m,pixel)\cdot T_m(m)}{\sum_{m=1}^{12} M_{70}(m,pixel)\cdot T_m(m)} \end{aligned} \tag{4}$$

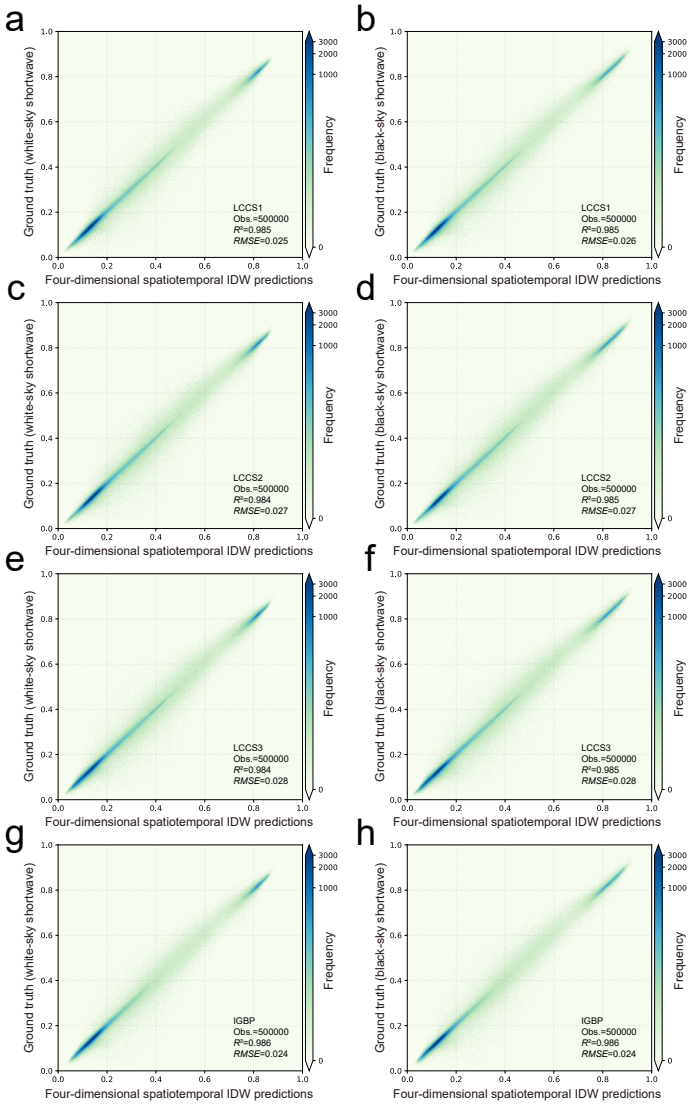
where A_{GL} is the global land area (147.9 million km^2). N_{pixel} is the number of pixels in the global land. A_{pixel} is the area of each pixel. $M_{70}=0$ if the maximum solar zenith angle of the day is greater than 70°; otherwise, $M_{70}=1$. T_m denotes one month with units of seconds in a normal year.

The global mean radiative forcing resulting from the above albedo change is estimated by using Eq. (5).

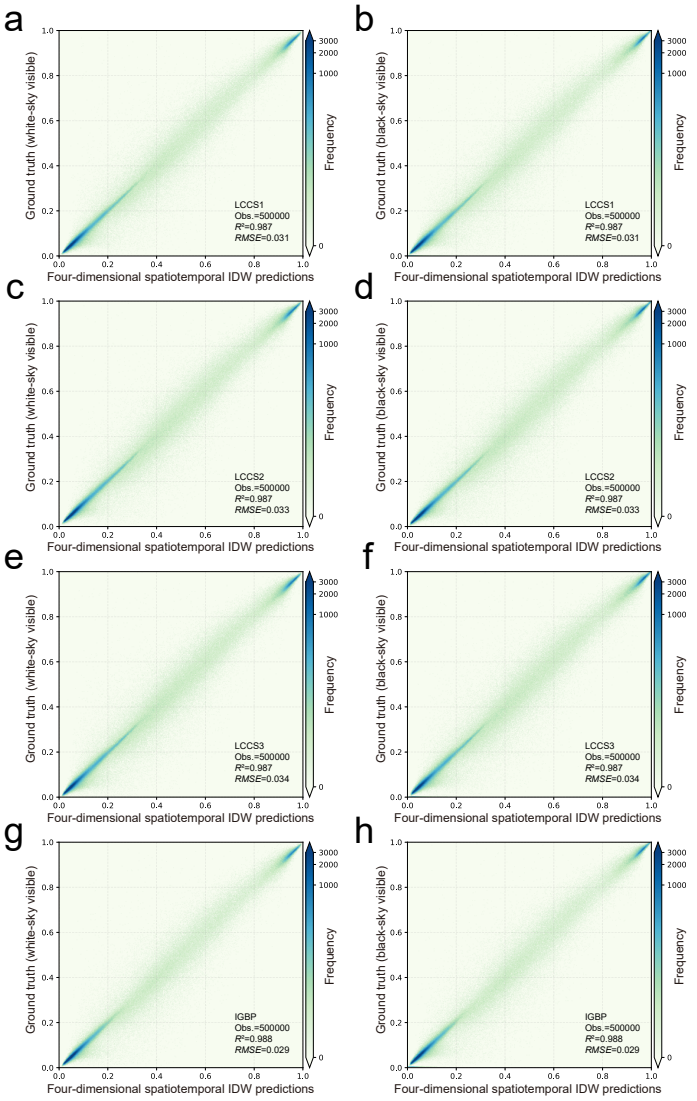
$$\begin{aligned} &GMRF^{Z} = \frac{100}{A_{global}\cdot T_y}\cdot \sum_{pixel=1}^{N_{pixel}}\sum_{m=1}^{12} \\ &[C^{Z}_{\alpha-pixel}(m,p,blue)\cdot A_{pixel}(p)\cdot K_r(m,p)\cdot M_{85}(m,p)\cdot T_m(m)] \end{aligned} \tag{5}$$

where $K_r(m, p)$ denotes the shortwave radiation kernel (W/m^2) for each month, and is resampled to 500m-resolution pixels, A_{global} is the global surface area (510 million km^2). $M_{85} = 0$ if the maximum solar zenith angle of the day is greater than 85°; otherwise, $M_{85} = 1$. Ty denotes one normal year with units of seconds. The value of 100 is used to account for the kernel definition for every 0.01 change in surface albedo.

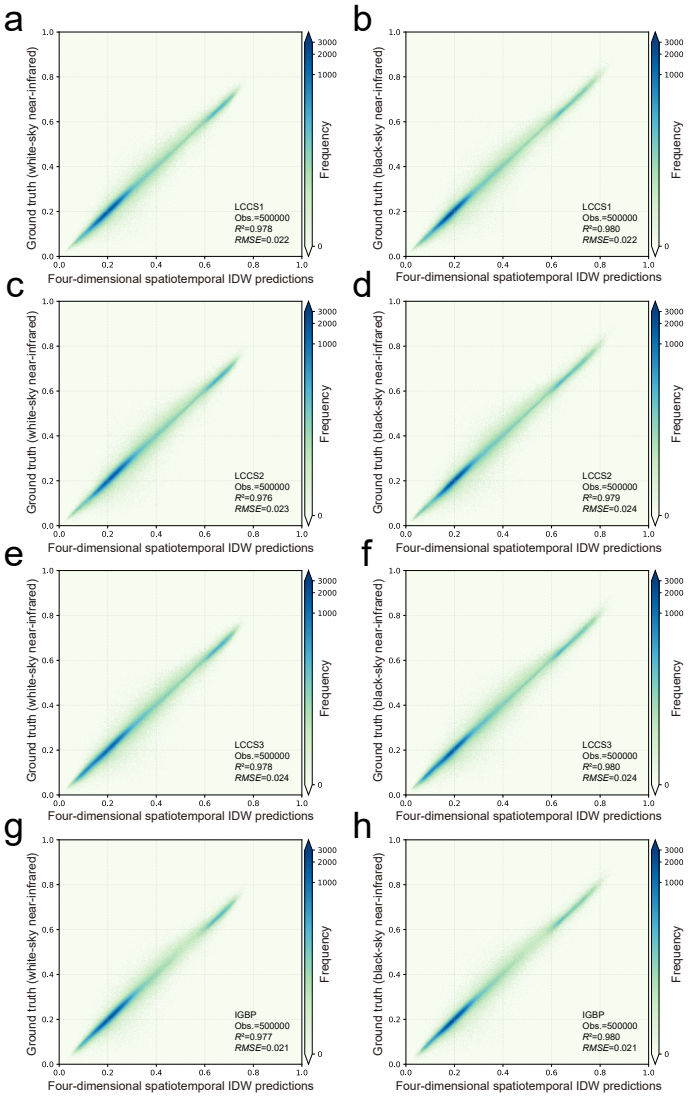
2 Supplementary Figures



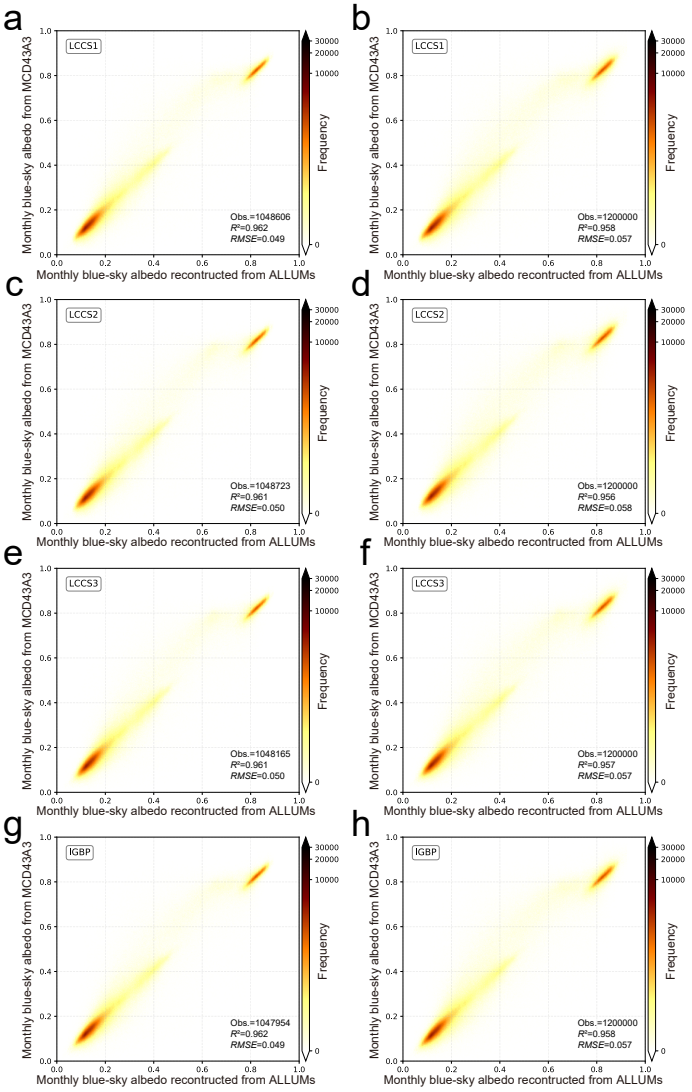
Supplementary Fig. S1 | Validation of the four-dimensional spatiotemporal IDW interpolation for shortwave albedo. White-sky shortwave albedo **(a, c, e, g)** and black-sky shortwave albedo **(b, c, f, h)** in ALLUM-LCCS 1 **(a, b)**, ALLUM-LCCS 2 **(c, d)**, ALLUM-LCCS 3 **(e, f)** and ALLUM-IGBP **(g, h)**.



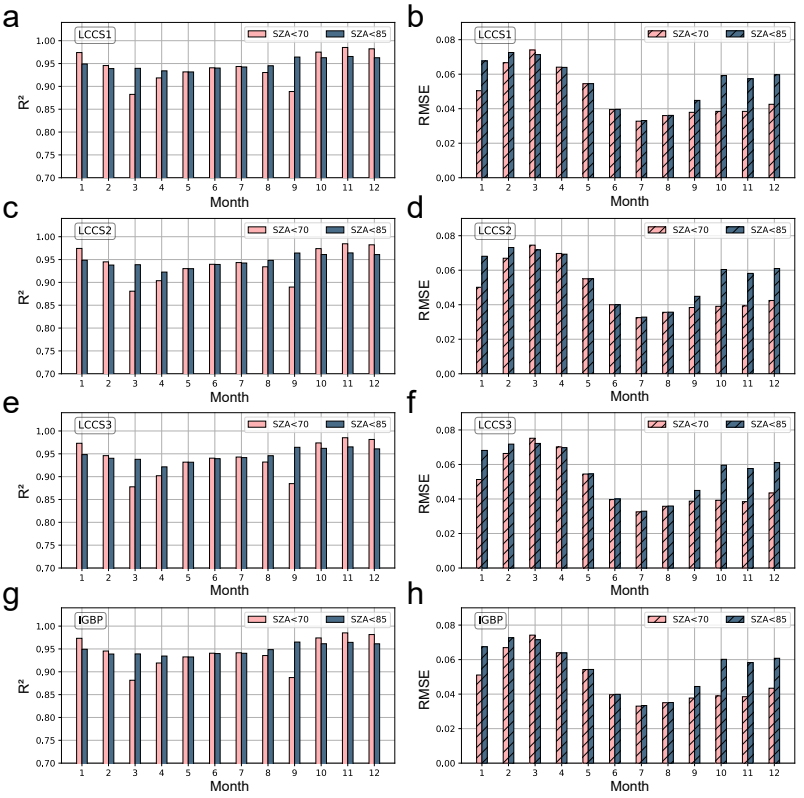
Supplementary Fig. S2 | Validation of the four-dimensional spatiotemporal IDW interpolation for visible albedo. White-sky visible albedo **(a, c, e, g)** and black-sky visible albedo **(b, c, f, h)** in ALLUM-LCCS 1 **(a, b)**, ALLUM-LCCS 2 **(c, d)**, ALLUM-LCCS 3 **(e, f)** and ALLUM-IGBP **(g, h)**.



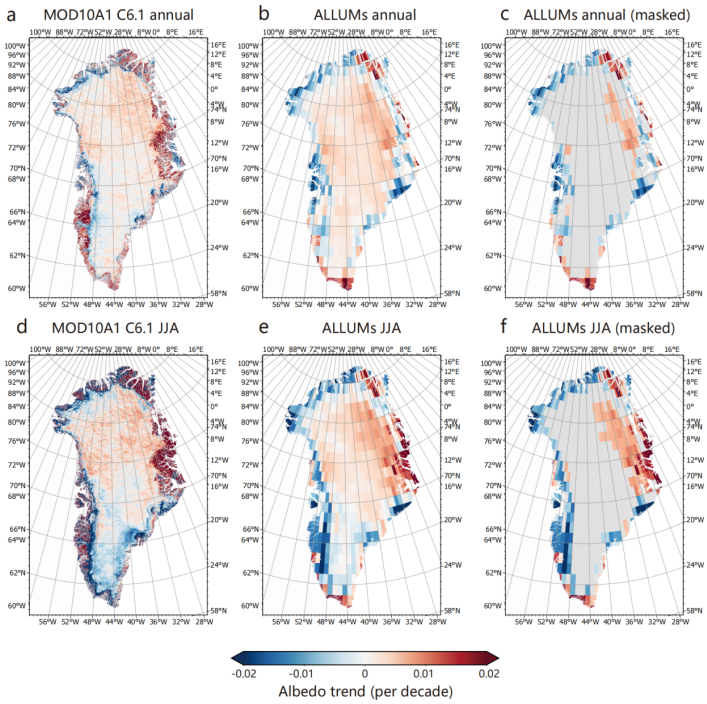
Supplementary Fig. S3 | Validation of the four-dimensional spatiotemporal IDW interpolation for near-infrared albedo. White-sky near-infrared albedo **(a, c, e, g)** and black-sky **(b, c, f, h)** near-infrared albedo in ALLUM-LCCS 1 **(a, b)**, ALLUM-LCCS 2 **(c, d)**, ALLUM-LCCS 3 **(e, f)** and ALLUM-IGBP **(g, h)**.



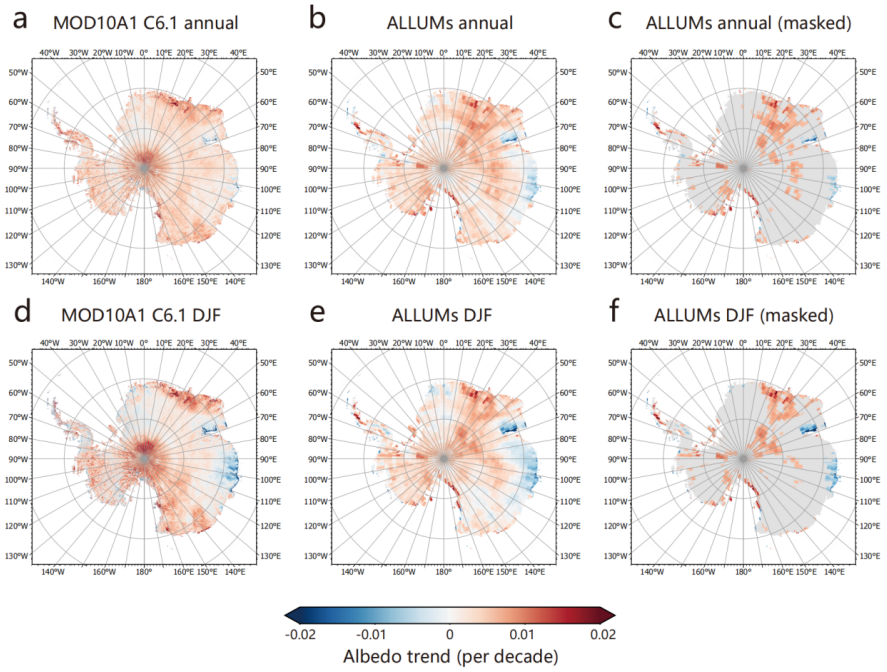
Supplementary Fig. S4 | Validation of 500m-resolution albedo reconstruction from ALLUMs. The regions less than 70° in the solar zenith angle **(a, c, e, g)** and the regions less than 85° in the solar zenith angle **(b, d, f, h)** for ALLUM-LCCS 1 **(a, b)**, ALLUM-LCCS 2 **(c, d)**, ALLUM-LCCS 3 **(e, f)** and ALLUM-IGBP **(g, h)**.



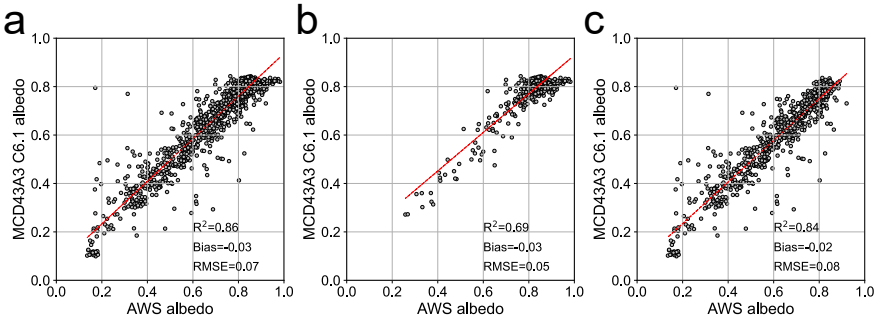
Supplementary Fig. S5 | Validation of 500m-resolution albedo reconstruction from ALLUMs. r^2 value for individual months **(a, c, e, g)** and RMSE values **(b, d, f, h)** are shown for ALLUM-LCCS 1 **(a, b)**, ALLUM-LCCS 2 **(b, c)**, ALLUM-LCCS 3 **(e, f)** and ALLUM-IGBP **(g, h)**, comparing the regions with Solar Zenith Angles (SZA) $<70°$ and $<85°$. For each month, the 500m-resolution albedo reconstruction is a weighted combination of snow albedo and snow-free albedo based on snow fraction, while MCD43A3 C6.1 monthly mean albedo is calculated as the average of daily snow and snow-free albedo per pixel. In the snow-covered regions, differences in the two data generation methods can cause large inconsistencies during some seasons. Limited daily data availability may affect the snow albedo and snow-free albedo proportions in the MCD43A3 C6.1 monthly average synthesis data. The associated uncertainty is mitigated by our reconstruction method.



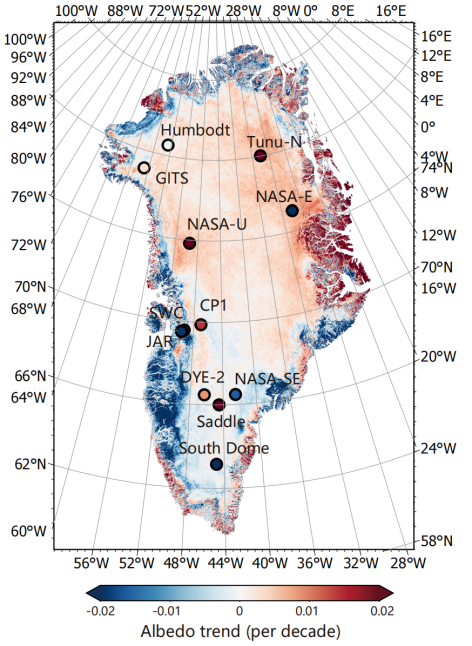
Supplementary Fig. S6 | Decadal snow albedo trends over Greenland during 2001–2020. Panels (**a, d**) display trends for MOD10A1 C6.1, while panels (**b, c, e, f**) illustrate to ALLUMs. Panels (**a, b**) show the annual mean snow albedo changes, while panels (**d, e**) focus on albedo changes in June–August. Panels (**c, f**) mask regions where albedo changes fall below the calibration error (gray areas). The used calibration error is 0.7% per decade, as detailed in Supplementary Text 4.



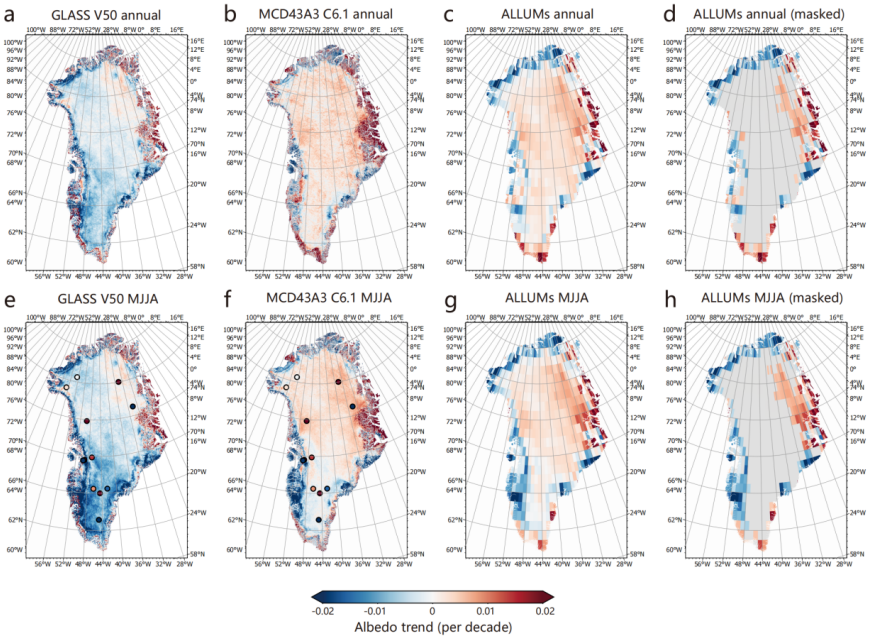
Supplementary Fig. S7 | Decadal albedo change trends over Antarctica during 2001–2020. Panels (**a, d**) display trends for MOD10A1 C6.1, while panels (**b, c, e, f**) illustrate to ALLUMs. Panels (**a, b**) show annual trends calculated using albedo values for all months, while panels (**d, e**) show trends based on June–August albedo. Panels (**c, f**) mask regions where albedo changes fall below the calibration error (gray areas). The calibration error is 0.7% per decade, as detailed in Supplementary Text 4.



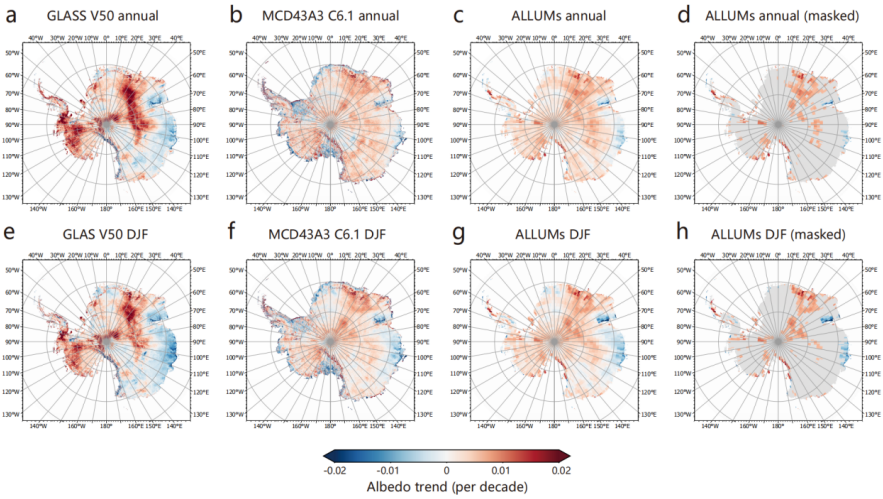
Supplementary Fig. S8 | Comparisons of MCD43A3 C6.1 albedo data with ground-based observations from GC-Net/PROMICE AWS stations. Panel (**a**) includes data from all 38 GC-Net/PROMICE AWS stations established before 2021. Panel (**b**) focuses on 12 GC-Net AWS stations established before 2001, while panel (**c**) covers 26 GC-Net/PROMICE AWS stations established during 2001–2020.



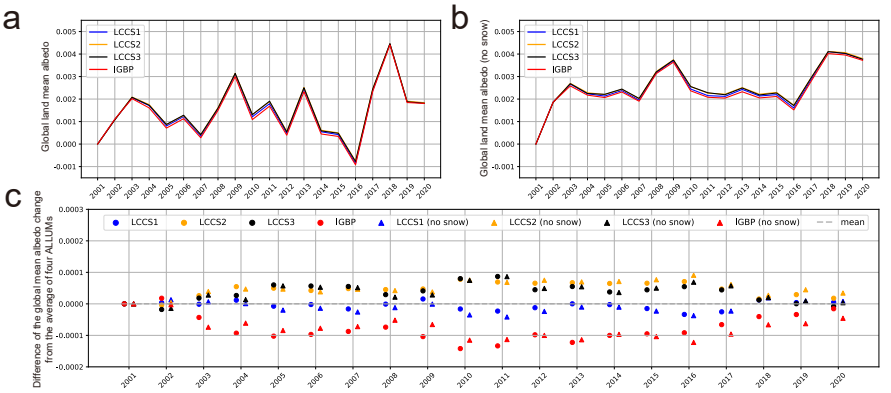
Supplementary Fig. S9 | Albedo trends at 12 GC-Net stations over Greenland compared with the MCD43A3 C6.1 data for May-August from 2001 to 2020.



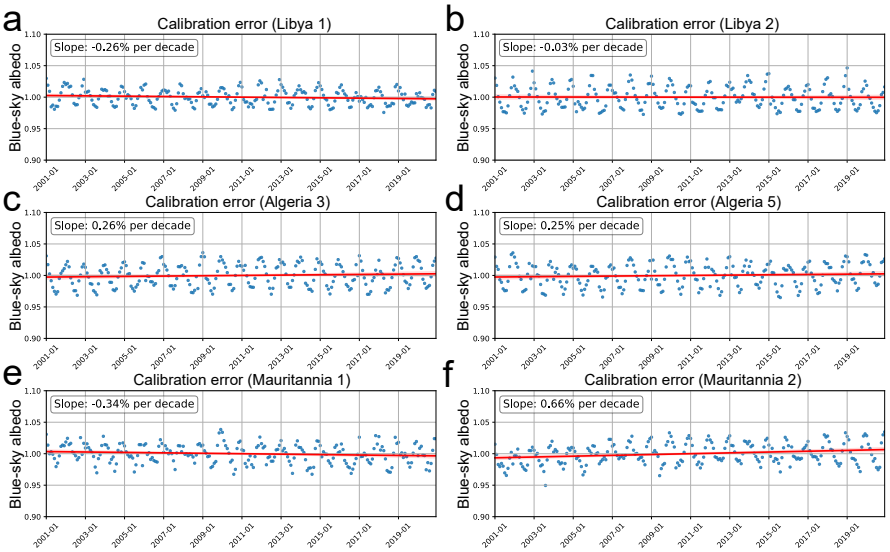
Supplementary Fig. S10 | Decadal albedo change trends (including snow and snow-free regions) over Greenland from 2001 to 2020. Panels (**a, e**) display trends for GLASS02B03, panels (**b, f**) for MCD43A3 C6.1, and panels (**c, d, g, h**) for ALLUMs. The trends in (**a**)-(**d**) are calculated using the annual mean albedo values for all months over the 20-year period, while the trends in (**e-h**) are synthesized only using the albedo data from May to August. Panels (**d-h**) show the trends with the areas where the albedo change is smaller than the calibration error are masked (gray). The calibration error used is 0.7% per decade, as detailed in Supplementary Text 4.



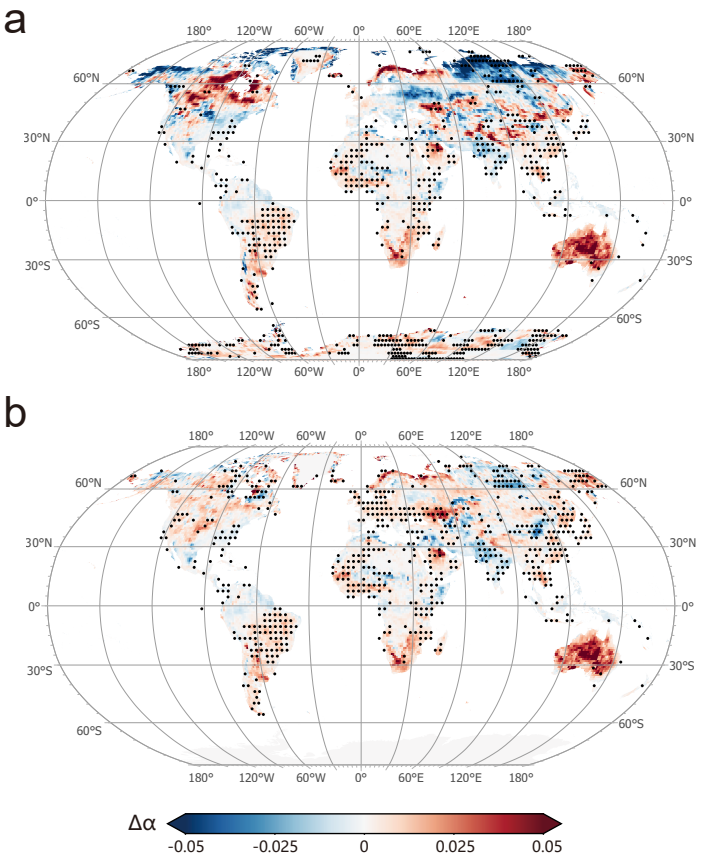
Supplementary Fig. S11 | Decadal albedo change trends (including snow and snow-free regions) over the Antarctica from 2001 to 2020. Panels (**a, e**) display trends for GLASS02B03, panels (**b, f**) for MCD43A3 C6.1, and panels (**c, d, g, h**) for ALLUMs. The trends in panels (**a-d**) are calculated using the annual mean albedo values for all months over the 20-year period, while the trends in panels (**e-h**) are synthesized only using the albedo data from December to February. Panels (**d-h**) show the trends with the areas where the albedo changes are smaller than the calibration error are masked (gray). The used calibration error is 0.7% per decade, as detailed in Supplementary Text 4.



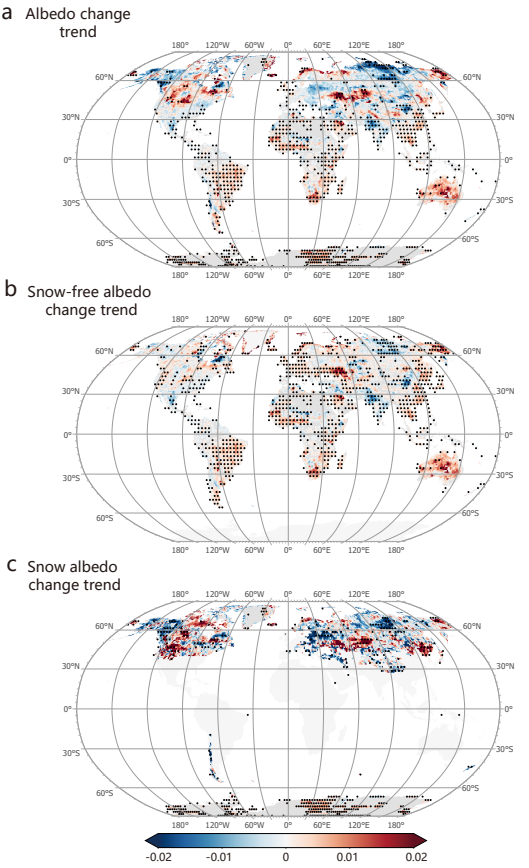
Supplementary Fig. S12 | Deviations of global land and snow-free land surface mean albedo changes across ALLUM-LCCS 1-3 and ALLUM-IGBP. a-b, Global land surface mean albedo changes in **(a)**, and snow-free land surface mean albedo changes in **(b)** derived from ALLUM-LCCS 1 (blue line), ALLUM-LCCS 2 (orange line), ALLUM-LCCS 3 (green line), and ALLUM-IGBP (red line). **c,** Deviations in the global land (circles) and snow-free land (triangles) surface mean albedo changes relative to the average of the four ALLUM datasets.



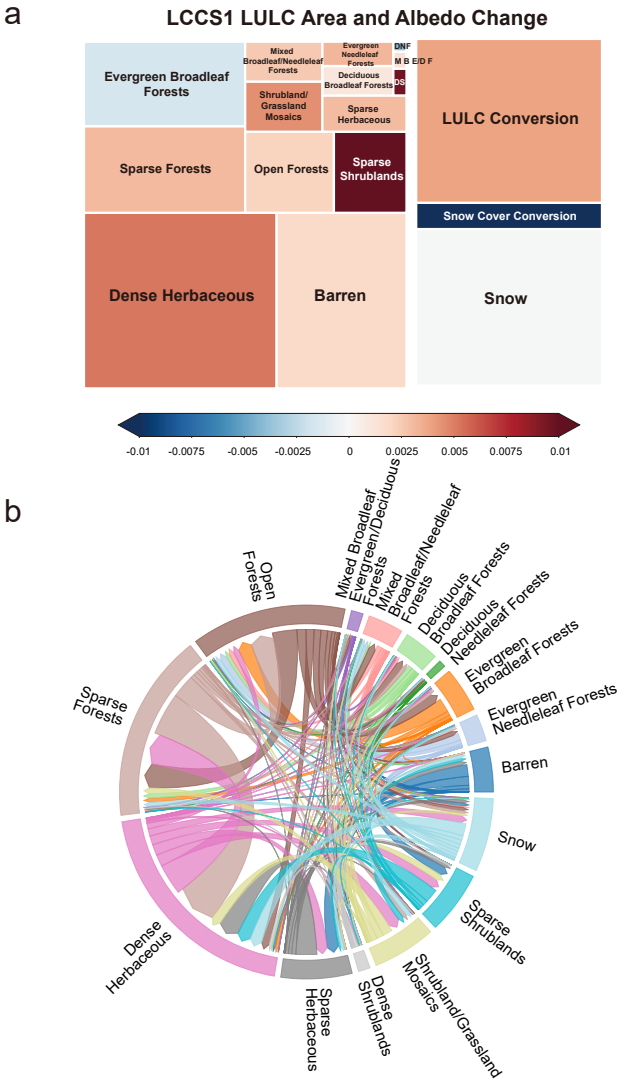
Supplementary Fig. S13 | Calibration trends of MCD43A3 C6.1 blue-sky albedo from 2001 to 2020 at six PICSs recognized by CEOS WGCV IVOS.



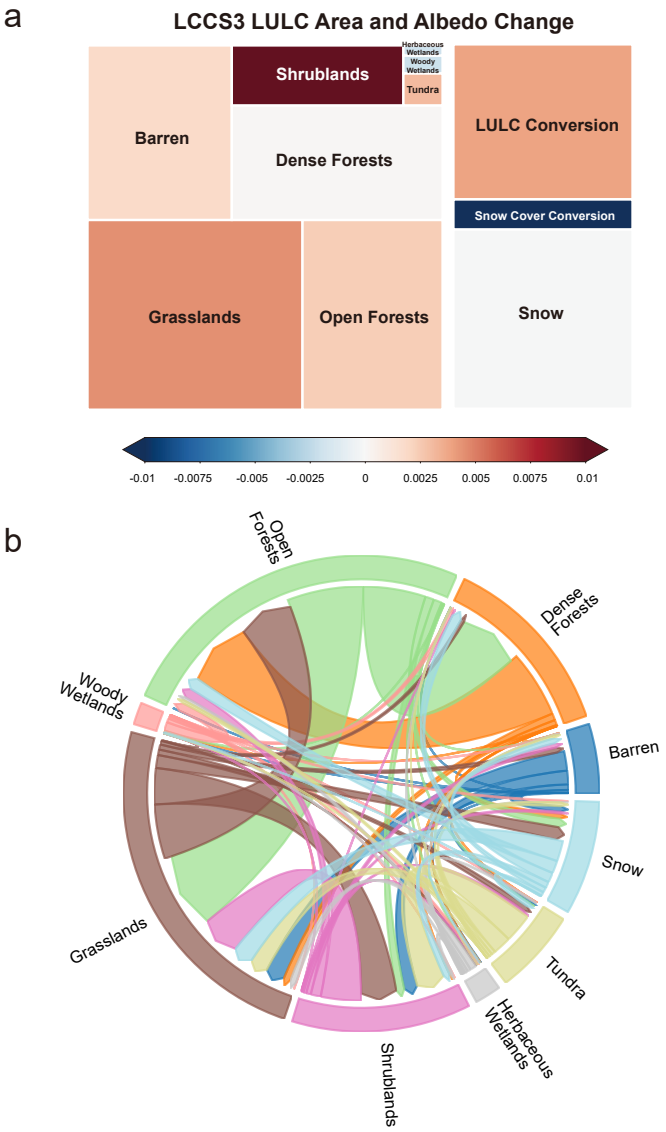
Supplementary Fig. S14 | Spatial distribution of absolute albedo changes from 2001 to 2020 after the calibration limit mask is applied. Panels a and b show global land surface albedo changes across all land and snow-free land after applying the calibration limit mask. Only grid cells where snow-free regions account for more than 5% of the land area are displayed in panel **b**. The black dots indicate the bins where the average albedo change between two independent temporal windows (2011-2020 and 2001-2010) is statistically significant (i.e., different from zero in two-sided Student's t-test; P-value $<$ 0.05). After the masked areas in the significance test are excluded, the areas with statistically significant change account for 19.5% of all areas in these grid cells (with 13.1% showing an increase and 6.4% showing a decrease) in panel **a**. The snow-free areas with statistically significant trends account for 26.3% of all snow-free areas in the displayed grid cells (with 18.9% showing an increase and 7.4% showing a decrease) in panel **b**. These results represent the average calculated from ALLUM-LCCS 1-3 and ALLUM-IGBP. Significance tests are conducted within each 3°×3° grid cell for clear visualization. Fig. 1c and Extended Data Fig. 2a in the main text correspond to panels (**a-b**) showing albedo changes without applying the mask.



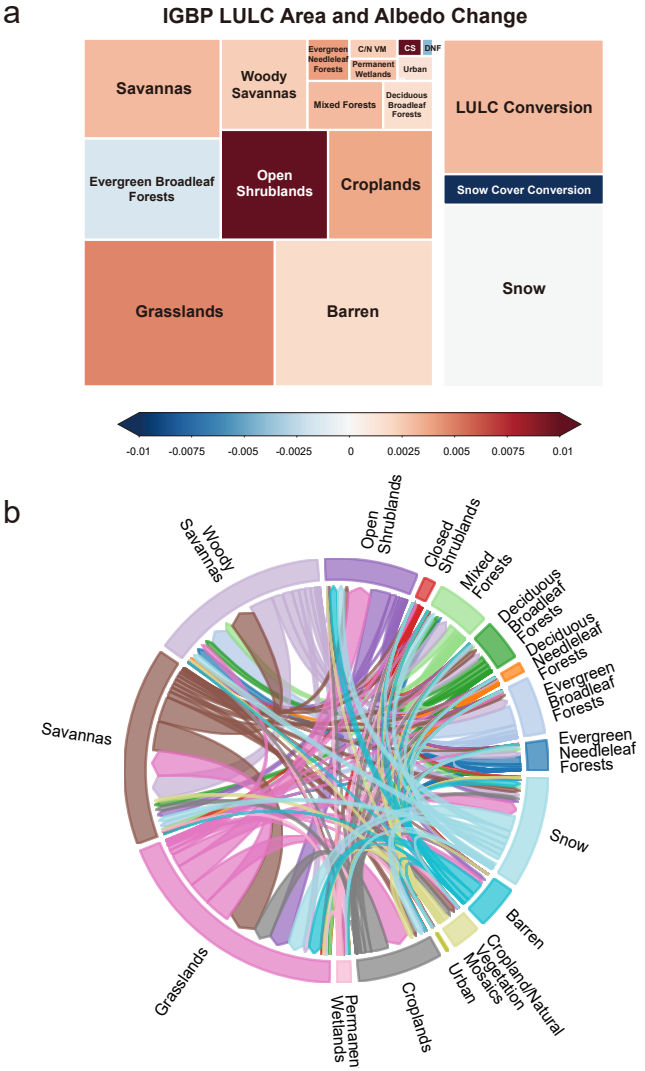
Supplementary Fig. S15 | Global albedo changes from 2001 to 2020 based on ALLUMs with the calibration mask applied.. Panel (**a**) shows albedo changes in global land areas, while panels (**b**) and (**c**) illustrate changes in snow-free and snow-covered regions, respectively. The linear trend in each grid cell is regressed using the Theil-Sen Median method as a robust statistical approach. The black dots indicate statistically significant trends determined by the Mann-Kendall test (P-value < 0.05). The trends in the areas where the albedo change is smaller than the calibration error are masked (gray). The used calibration error is 0.7% per decade, as detailed in Supplementary Text 4. After the masked areas in the significance test are excluded, the areas with statistically significant trends account for 25.9% of the global land surface areas in panel a (with 18.6% showing an increase and 7.5% showing a decrease). In panel **b** and **c**, only grid cells where snow-free regions and snow regions account for more than 5% of the grid cell land area are displayed, respectively. The snow-free areas with statistically significant trends account for 35.3% of all snow-free areas in these grid cells (with 26.8% showing an increase and 8.5% showing a decrease); and the snow-covered areas with statistically significant trends account for 16.1% of all snow areas in the displayed grid cells (with 11.4% showing an increase and 4.7% showing a decrease). These results represent the mean albedo changes derived from ALLUM-LCCS 1-3 and ALLUM-IGBP datasets. Significance tests are conducted in each 3°×3° grid cell for clear visualization. Fig. 1b and Extended Data Fig. 2b in the main text, and Fig. S22 correspond to panels **a**–**c** showing albedo changes without applying the mask.



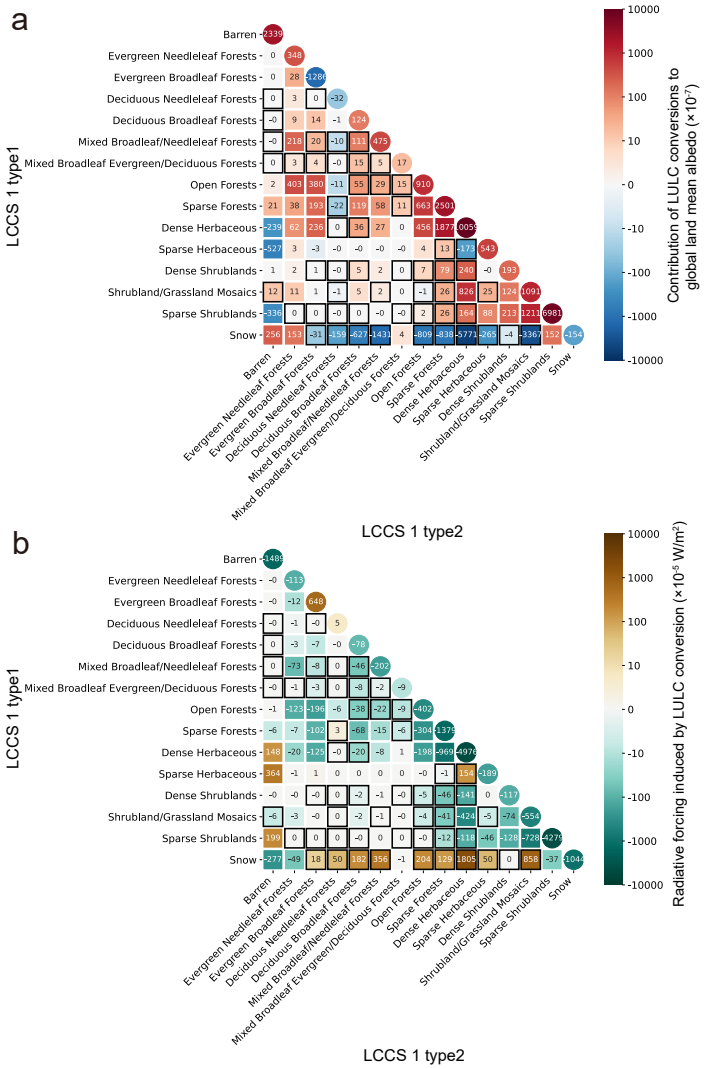
Supplementary Fig. S16 | Global LULC and albedo changes under LCCS 1. a, Albedo changes across all regions, with and without LULC conversions defined by LCCS 1. The area of each rectangle represents the proportion of land occupied by the specific LULC type, and the color indicates the change in albedo. M B E/D F, DNF and DS denote Mixed Broadleaf Evergreen/Deciduous Forests, Deciduous Needleleaf Forests and Sparse Shrublands, respectively. **b,** Areas of LULC conversions through 210 conversion pathways. The arc length represents the area of LULC conversion regions associated with the corresponding LULC type t. Inward arrows show conversions from other LULC types to t, while the outward arrows indicate conversions from t to other types. The thickness of the arrows indicates reflects the size of the conversion area.



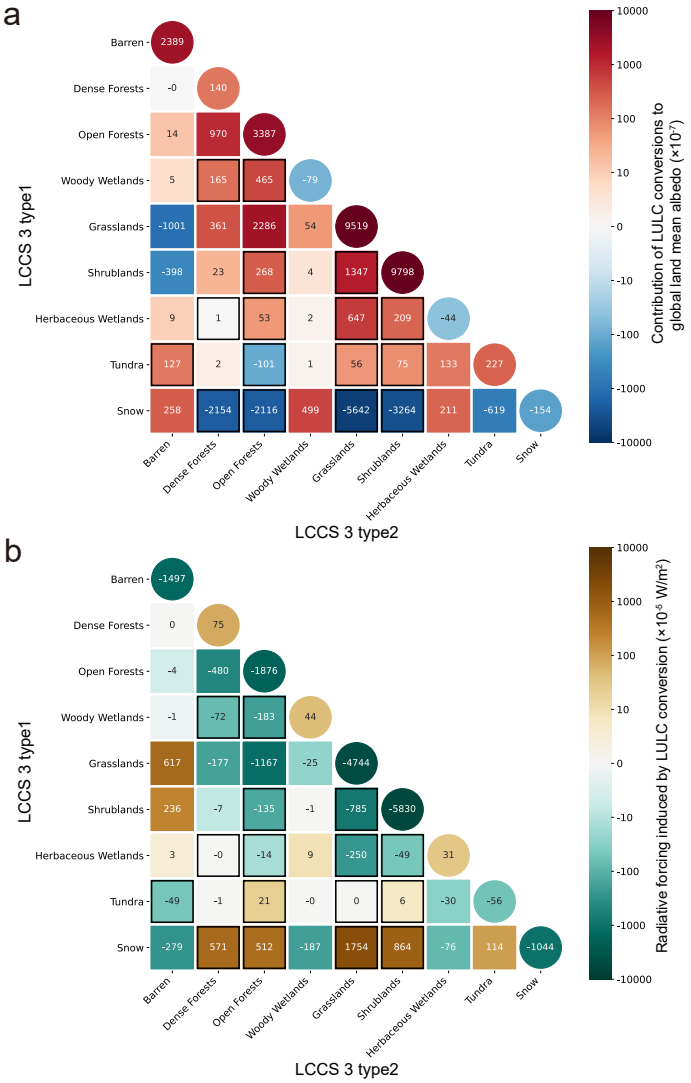
Supplementary Fig. S17 | Global LULC and albedo changes under LCCS 3. a, Albedo changes across all regions, with and without LULC conversions defined by LCCS 3. The area of each rectangle represents the proportion of land occupied by the specific LULC type, and the color indicates the change in albedo. **b,** Areas of LULC conversions through 72 conversion pathways. The arc length represents the area of LULC conversion regions associated with the corresponding LULC type t. Inward arrows show conversion from other LULC types to t, while the outward arrows represent conversion from t to other types. The thickness of the arrows indicates reflects the size of the conversion area.



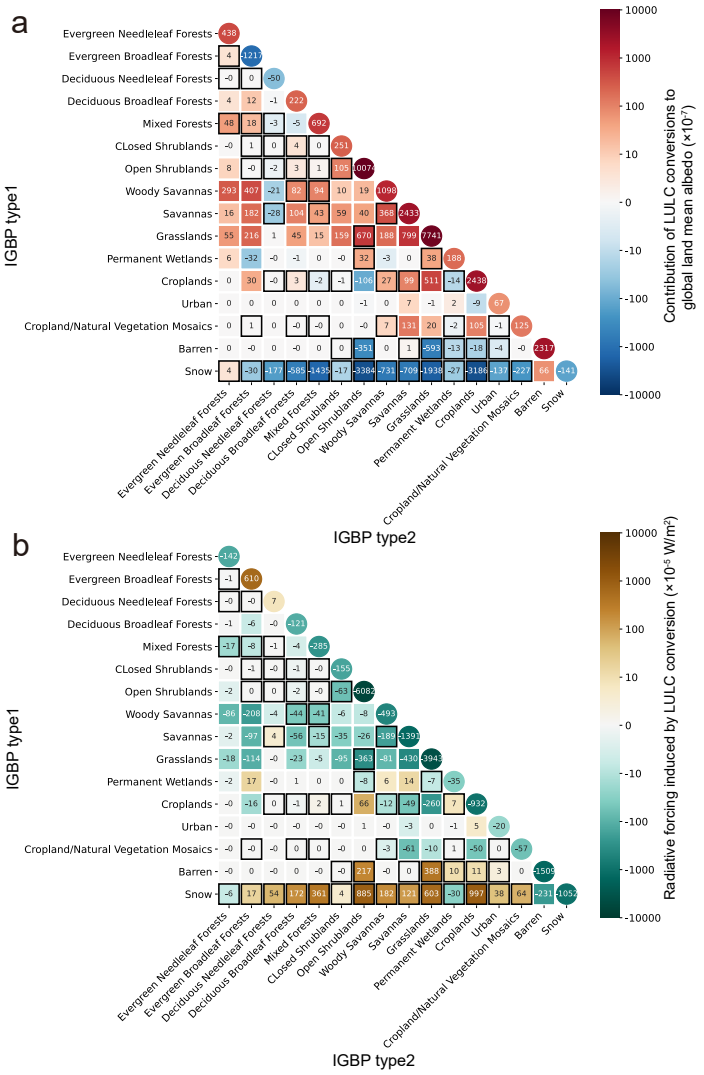
Supplementary Fig. S18 | Global LULC and albedo changes under IGBP. a, Albedo changes across all regions, with and without LULC conversions defined by IGBP. The area of each rectangle represents the proportion of land occupied by the specific LULC type, and the color indicates the change in albedo. CS and DNF denote Closed Shrublands and Deciduous Needleleaf Forests, respectively. **b,** Areas of LULC changes through 240 conversion pathways. The arc length represents the area of LULC conversion regions associated with the corresponding LULC type t. Inward arrows show conversions from other LULC types to t, while the outward arrows indicate conversions from t to other types. The thickness of the arrows reflects the size of the conversion area.



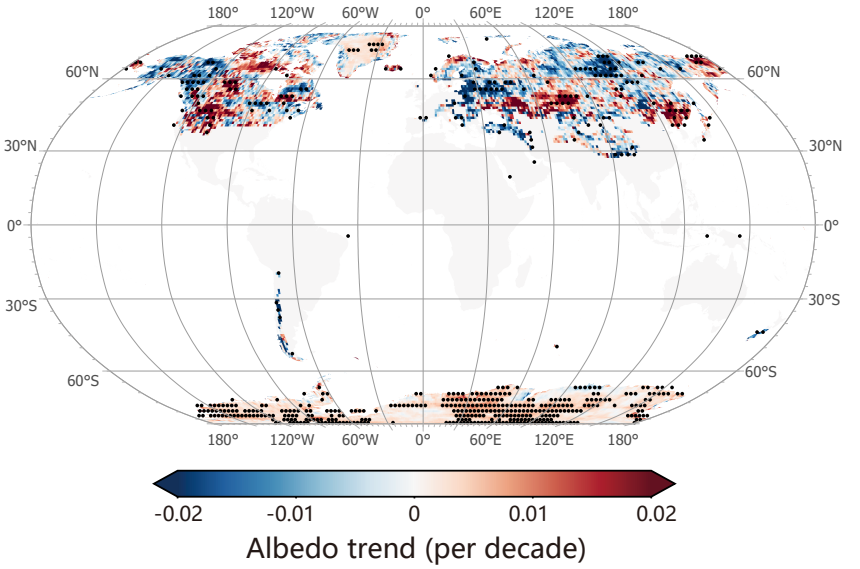
Supplementary Fig. S19 | The global land mean albedo change and global land mean radiative forcing resulting from each net bidirectional LULC conversion and each LULC non-conversion region defined by LCCS 1. a, The global land surface mean albedo change. For each square or circle, the color and the number inside represent the magnitude of the global land surface mean albedo increase. The black outline denotes the net conversion from LULC type 1 to type 2; otherwise, it indicates the net conversion from type 2 to type 1. Circles denote contributions from LULC non-conversion regions. **b,** as panel **(a)** but for albedo-induced global mean radiative forcing. For each square or circle, the color and the number inside represent the magnitude of radiative forcing.



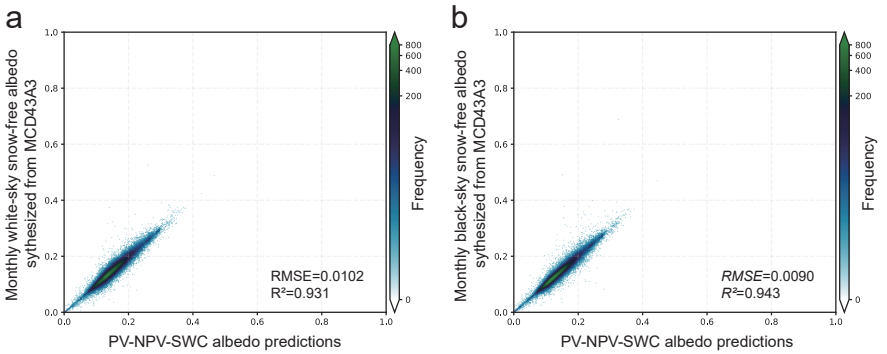
Supplementary Fig. S20 | The global land mean albedo change and global land mean radiative forcing resulting from each net bidirectional LULC conversion and each LULC non-conversion region defined by LCCS 3. a, The global land surface mean albedo change. For each square or circle, the color and the number inside represent the magnitude of the global land surface mean albedo increase. The black outline denotes the net conversion from LULC type 1 to type 2; otherwise, it indicates the net conversion from type 2 to type 1. Circles denote contributions from LULC non-conversion regions. **b,** as panel **(a)** but for albedo-induced global mean radiative forcing. For each square or circle, the color and the number inside represent the magnitude of radiative forcing.



Supplementary Fig. S21 | The global land mean albedo change and global land mean radiative forcing resulting from each net bidirectional LULC conversion and each LULC non-conversion region defined by IGBP. a, The global land surface mean albedo change. For each square or circle, the color and the number inside represent the magnitude of the global land surface mean albedo increase. The black outline denotes the net conversion from LULC type 1 to type 2; otherwise, it indicates the net conversion from type 2 to type 1. Circles denote contributions from LULC non-conversion regions. **b,** as panel **(a)** but for albedo-induced global mean radiative forcing. For each square or circle, the color and the number inside represent the magnitude of radiative forcing.

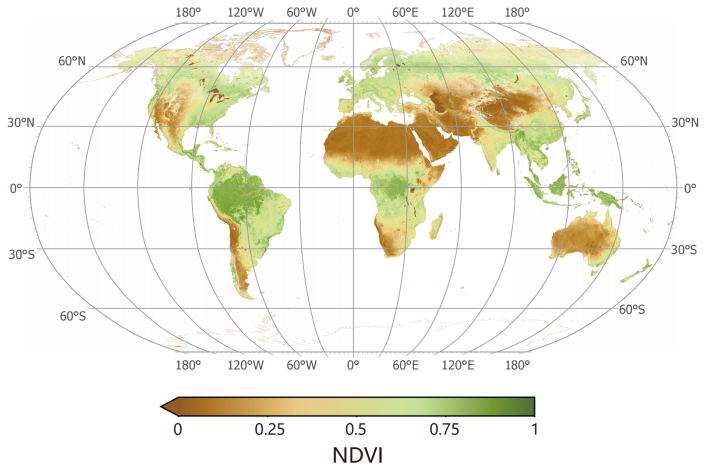


Supplementary Fig. S22 | Global land surface snow albedo changesfrom 2001 to 2020. The linear trend for each grid cell is regressed using the Theil-Sen Median method as a robust statistical approach. The black dots indicate statistically significant trends determined by the Mann-Kendall test (P-value < 0.05). Only the grid cells where snow covered regions account for more than 5% of the grid cell land area are displayed. The snow-covered areas with statistically significant trends account for 33.9% of all snow area in these grid cells (with 29.1% showing an increase and 4.8% showing a decrease). These results represent the average albedo changes derived from ALLUM-LCCS 1-3 and ALLUM-IGBP datasets. Significance tests are conducted within each 3°×3° grid cell for clear visualization.

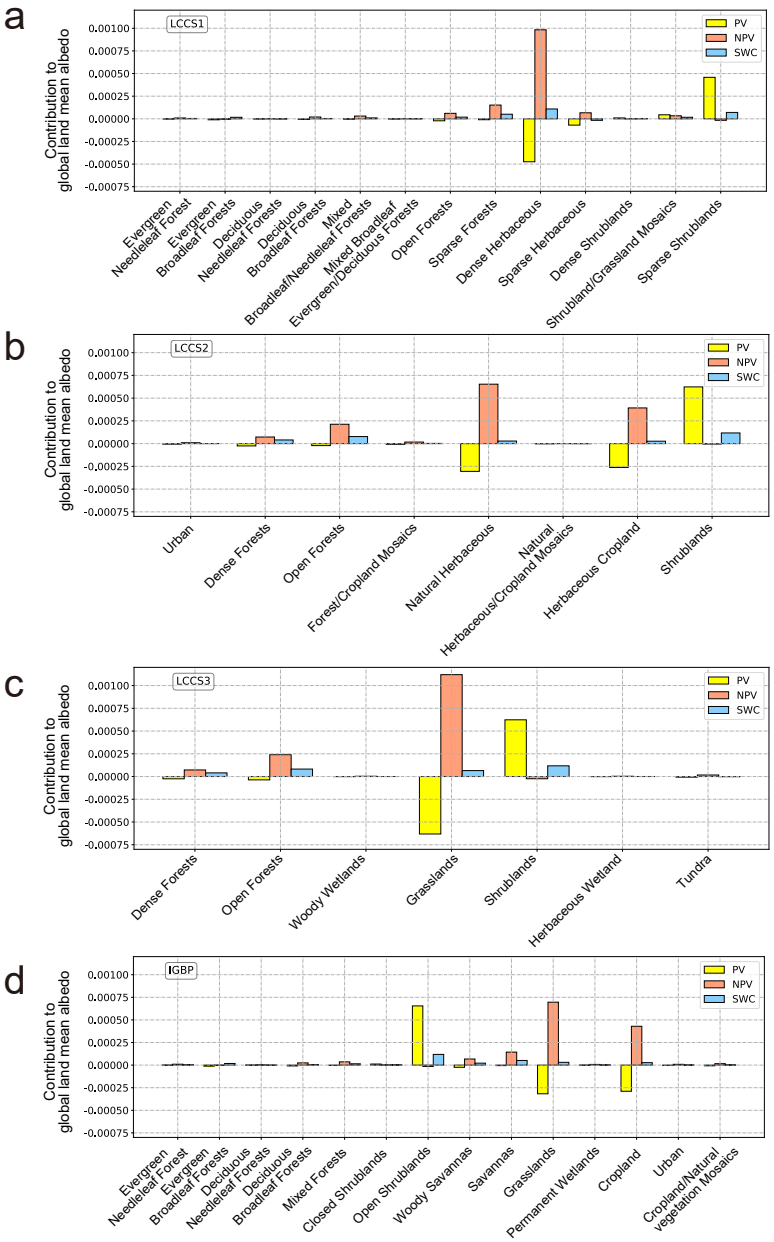


527

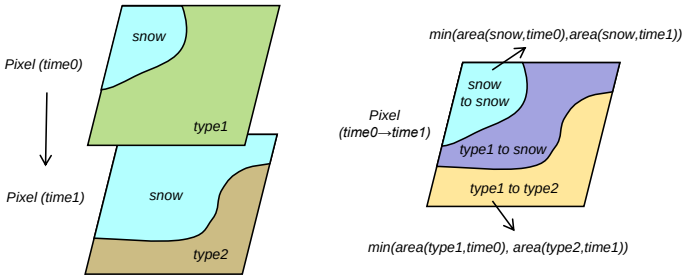
528 **Supplementary Fig. S23 | Validations of albedo predicted by the PV-NPV-SWC**
529 **model regression. a,** White-sky shortwave albedo. **b,** Black-sky shortwave albedo.



Supplementary Fig. S24 | The normalized difference vegetation index (NDVI) for the year 2020.



Supplementary Fig. S25 | Contributions of PV, NPV, and SWC to global land surface mean albedo change in LULC non-conversion regions. Panels (**a-d**) display the contributions of PV, NPV, and SWC to global land surface mean albedo change in LULC non-conversion regions for LCCS 1, LCCS 2, LCCS 3, and IGBP, respectively.



Supplementary Fig. S26 | The schematic diagram for calculating the areas of LULC conversions within a pixel.

3 Supplementary Tables

Supplementary Table S1 | The 15 land cover classes defined by LCCS 1[25, 26]. Water bodies (3) are excluded in our analysis. The classes are derived from the MODIS/Terra+Aqua Land Cover Dataset, with class numbers shown in parentheses next to the class name[27, 28].

Name	Description
Barren (1)	At least 60% of area is non-vegetated barren (sand, rock, soil) or permanent snow/ice with less than 10% vegetation.
Permanent Snow and Ice (2)	At least 60% of area is covered by snow and ice for at least 10 months of the year.
Evergreen Needleleaf Forests (11)	Dominated by evergreen conifer trees (>2m). Tree cover >60%.
Evergreen Broadleaf Forests (12)	Dominated by evergreen broadleaf and palmate trees (>2m). Tree cover >60%
Deciduous Needleleaf Forests (13)	Dominated by deciduous needleleaf (larch) trees (>2m). Tree cover >60%.
Deciduous Broadleaf Forests (14)	Dominated by deciduous broadleaf trees (>2m). Tree cover >60%.
Mixed Broadleaf/Needleleaf Forests (15)	Co-dominated (40-60%) by broadleaf deciduous and evergreen needleleaf tree (>2m) types. Tree cover >60%.
Mixed Broadleaf Evergreen/Deciduous Forests (16)	Co-dominated (40-60%) by broadleaf evergreen and deciduous tree (>2m) types. Tree cover >60%.
Open Forests (21)	Co-dominated (40-60%) by broadleaf evergreen and deciduous tree (>2m) types. Tree cover >60%.
Sparse Forests (22)	Tree cover 30-60% (canopy >2m).
Dense Herbaceous (31)	Dominated by herbaceous annuals (<2m) at least 60% cover.
Sparse Herbaceous (32)	Dominated by herbaceous annuals (<2m) 10-60% cover.
Dense Shrublands (41)	Dominated by woody perennials (1-2m) >60% cover.
Shrubland/Grassland Mosaics (42)	Dominated by woody perennials (1-2m) 10-60% cover with dense herbaceous annual understory
Sparse Shrublands (43)	Dominated by woody perennials (1-2m) 10-60% cover with minimal herbaceous understory.

Supplementary Table S2 | The 9 land cover classes defined by LCCS 2[25, 26]. Water bodies (3) are excluded in our analysis. The classes are derived from the MODIS/Terra+Aqua Land Cover Dataset, with class numbers shown in parentheses next to the class name[27, 28].

Name	Description
Barren (1)	At least 60% of area is non-vegetated barren (sand, rock, soil) or permanent snow/ice with less than 10% vegetation.
Permanent Snow and Ice (2)	At least 60% of area is covered by snow and ice for at least 10 months of the year.
Urban and Built-up Lands (9)	At least 30% of area is made up of impervious surfaces including building materials, asphalt, and vehicles.
Dense Forests (10)	Tree cover >60% (canopy >2m).
Open Forests (20)	Tree cover 10-60% (canopy >2m).
Forest/Cropland Mosaics (25)	Mosaics of small-scale cultivation 40-60% with >10% natural tree cover.
Natural Herbaceous (30)	Dominated by herbaceous annuals (<2m). At least 10% cover.
Natural Herbaceous/Croplands Mosaics (35)	Mosaics of small-scale cultivation 40-60% with natural shrub or herbaceous vegetation.
Herbaceous Croplands (36)	Dominated by herbaceous annuals (<2m). At least 60% cover. Cultivated fraction >60%.
Shrublands (40)	Shrub cover >60% (1-2m).

Supplementary Table S3 | The 10 land cover classes defined by LCCS 3[25, 26]. Water bodies (3) are excluded in our analysis. The classes are derived from the MODIS/Terra+Aqua Land Cover Dataset, with class numbers shown in parentheses next to the class name[27, 28].

Name	Description
Barren (1)	At least 60% of area is non-vegetated barren (sand, rock, soil) or permanent snow/ice with less than 10% vegetation.
Permanent Snow and Ice (2)	At least 60% of area is covered by snow and ice for at least 10 months of the year.
Dense Forests (10)	Tree cover >60% (canopy >2m).
Open Forests (20)	Tree cover 10-60% (canopy >2m).
Woody Wetlands (27)	Shrub and tree cover >10% (>1m). Permanently or seasonally inundated
Gresslands (30)	Dominated by herbaceous annuals (<2m) >10% cover.
Shrublands (40)	Shrub cover >60% (1-2m).
Herbaceous Wetlands (50)	Dominated by herbaceous annuals (<2m) >10% cover. Permanently or seasonally inundated.
Tubdra (51)	Tree cover <10%. Snow-covered for at least 8 months of the year.

Supplementary Table S4 | The 16 land cover classes defined by IGBP[29]. Water bodies (16) are excluded in our analysis. The classes are from the MODIS/Terra+Aqua Land Cover Dataset, with the class number in parentheses next to the class name[27, 28].

Name	Description
Evergreen Needleleaf Forests (1)	Lands dominated by woody vegetation with a percent cover >60% and height exceeding 2 meters. Almost of the trees remain green all year. Canopy is never without green foliage.
Evergreen Broadleaf Forests (2)	Lands dominated by woody vegetation with a percent cover >60% and height exceeding 2 meters. Almost all trees and shrubs remain green year-round. Canopy is never without green foliage.
Deciduous Needleleaf Forests (3)	Lands dominated by woody vegetation with a percent cover >60% and height exceeding 2 meters. Consists of seasonal needleleaf tree communities with an annual cycle of leaf-on and leaf-off periods.
Deciduous Broadleaf Forests (4)	Lands dominated by woody vegetation with a percent cover >60% and height exceeding 2 meters. Consists of broadleaf tree communities with an annual cycle of leaf-on and leaf-off periods.
Mixed Forests (5)	Lands dominated by trees with a percent cover ¿60% and height exceeding 2 meters. Consists of tree communities with interspersed mixtures or mosaics of the other four forest types. None of the forest types exceeds 60% of landscape.
Closed Shrublands (6)	Lands with woody vegetation less than 2 meters tall and with shrub canopy cover >60%. The shrub foliage can be either evergreen or deciduous.
Open Shrublands (7)	Lands with woody vegetation less than 2 meters tall and with shrub canopy cover between 10-60%. The shrub foliage can be either evergreen or deciduous.
Woody Savannas (8)	Lands with herbaceous and other understory systems, and with forest canopy cover between 30-60%. The forest cover height exceeds 2 meters.
Savannas (9)	Lands with herbaceous and other understory systems, and with forest canopy cover between 10-30%. The forest cover height exceeds 2 meters.
Grasslands (10)	Lands with herbaceous types of cover. Tree and shrub cover is less than 10%.
Permanent Wetlands (11)	Lands with a permanent mixture of water and herbaceous or woody vegetation. The vegetation can be present in either salt, brackish, or fresh water.
Croplands (12)	Lands covered with temporary crops followed by harvest and a bare soil period (e.g., single and multiple cropping systems). Note that perennial woody crops will be classified as the appropriate forest or shrub land cover type.
Urban and Built-up Lands (13)	Land covered by buildings and other man-made structures.

Name	Description
Cropland/Natural Vegetation Mosaics (14)	Lands with a mosaic of croplands, forests, shrubland, and grasslands in which no one component comprises more than 60% of the landscape.
Permanent Snow and Ice (15)	At least 60% of area is covered by snow and ice for at least 10 months of the year.
Barren (17)	Lands with exposed soil, sand, rocks, or snow and never has more than 10% vegetated cover during any time of the year.

Supplementary Table S5 | Methods to calculate the normalized NDVI, the spectral shape index (SSI) and the normalized multi-band drought index (NMDI).

Index	Methods
NDVI	$NDVI = \frac{band2-band1}{band2+band1}$
SSI	$SSI = \frac{slope_{nir-r}-slope_{g-b}}{slope_{nir-r}+slope_{g-b}}$
	$slope_{nir-r} = \frac{band2-band1}{WL_{band2}-WL_{band1}}$
	$slope_{g-b} = \frac{band4-band3}{WL_{band4}-WL_{band3}}$
NMDI	$NMDI = \frac{band2-(band6-band7)}{band2+(band6-band7)}$

Notes: *bands* 1-7 represent the surface reflectance of the corresponding bands for MOD09A1 C6.1. WL_{band} denotes the center wavelength of the corresponding band. The center wavelengths for bands 1-7 are 645μm, 858μm, 469μm, 555μm, 1,240μm, 1,640μm, and 2,130μm, respectively.

Supplementary Table S6 | The maping between the IGBP land cover classes and LUH land cover classes [19]

Land-use types in the LUH dataset	LULC types defined by IGBP
Primary lands	Evergreen Needleleaf Forests Evergreen Broadleaf Forests Deciduous Needleleaf Forests Deciduous Broadleaf Forests Mixed Forests Barren
Pasture Secondary lands	Closed Shrublands Open Shrublands Woody Savannas Savannas Grasslands Barren
Cropland	Croplands Cropland/Natural Vegetation Mosaicss
Urban	Urban and Built-up Lands
Wetlands	Permanent Wetlands

References

[1] Shepard, D.: A two-dimensional interpolation function for irregularly-spaced data. In: Proceedings of the 1968 23rd ACM National Conference, pp. 517–524. Association for Computing Machinery, New York, NY, USA (1968)

[2] Liu, Q., Wang, L., Qu, Y., Liu, N., Liu, S., Tang, H., Liang, S.: Preliminary evaluation of the long-term glass albedo product. International Journal of Digital Earth **6**, 69–95 (2013)

[3] Hall, D.K., Salomonson, V.V., Riggs, G.A.: MODIS/Terra Snow Cover Daily L3 Global 500m Grid. Version 6. figshare https://nsidc.org/data/mod10a1/versions/61 (2016)

[4] How, P., Abermann, J., Ahlstrøm, A.P., Andersen, S.B., Box, J.E., Citterio, M., Colgan, W.T., R.S., F., Karlsson, N.B., Jakobsen, J., Langley, K., Larsen, S.H., Lund, M.C., Mankoff, K.D., Pedersen, A., Rutishauser, A., Shield, C.L., Solgaard, A.M., van As, D., Vandecrux, B., Wright, P.J.: PROMICE and GC-Net automated weather station data in Greenland. GEUS Dataverse 20. figshare https://doi.org/10.22008/FK2/IW73UU (2022)

[5] Klein, A., Stroeve, J.C.: Development and validation of a snow albedo algorithm for the MODIS instrument. Annals of Glaciology **34**, 45–52 (2002)

[6] Burakowski, E.A., Ollinger, S.V., Lepine, L., Schaaf, C.B., Wang, Z., Dibb, J.E., Hollinger, D.Y., Kim, J., Erb, A., Martin, M.: Spatial scaling of reflectance and surface albedo over a mixed-use, temperate forest landscape during snow-covered periods. Remote Sensing of Environment **158**, 465–477 (2015)

[7] Tedesco, M., Doherty, S., Fettweis, X., Alexander, P., Jeyaratnam, J., Stroeve, J.: The darkening of the Greenland ice sheet: Trends, drivers, and projections (1981–2100). The Cryosphere **10**(2), 477–496 (2016)

[8] Casey, K.A., Polashenski, C.M., Chen, J., Tedesco, M.: Impact of MODIS sensor calibration updates on Greenland Ice Sheet surface reflectance and albedo trends. The Cryosphere **11**(4), 1781–1795 (2017)

[9] Sun, Y., Wang, Y., Zhai, Z., Zhou, M.: Changes in the Antarctic's Summer Surface Albedo, Observed by Satellite since 1982 and Associated with Sea Ice Anomalies. Remote Sensing **15**(20), 4940 (2023). https://doi.org/10.3390/rs15204940

[10] Ryan, J.C., Hubbard, A., Irvine-Fynn, T.D., Doyle, S.H., Cook, J.M.,

582 Stibal, M., Box, J.E.: How robust are in situ observations for validating
583 satellite-derived albedo over the dark zone of the Greenland Ice Sheet?
584 Geophysical Research Letters **44**(12), 6218–6225 (2017)

585 [11] Ye, F., Cheng, Q., Hao, W., Yu, D., Ma, C., Liang, D., Shen, H.: Recon-
586 structing daily snow and ice albedo series for Greenland by coupling
587 spatiotemporal and physics-informed models. International Journal of
588 Applied Earth Observation and Geoinformation **124**, 103519 (2023)

589 [12] Franz, B., Kwiatkowska, E., Meister, G., Mcclain, C.: Moderate reso-
590 lution imaging spectroradiometer on Terra: limitations for ocean color
591 applications. Journal of Applied Remote Sensing **2**(1), 023525 (2008)

592 [13] Xiong, X., Sun, J., Xie, X., Barnes, W.L., Salomonson, V.V.: On-orbit
593 calibration and performance of Aqua MODIS reflective solar bands. IEEE
594 Transactions on Geoscience and Remote Sensing **48**(1), 535–546 (2010)

595 [14] Lyapustin, A., Wang, Y., Xiong, X., Meister, G., Platnick, S., Levy, R.,
596 Franz, B., Korkin, S., Hilker, T., Tucker, J., Hall, F., Sellers, P., Wu, A.,
597 Angal, A.: Scientific impact of MODIS C5 calibration degradation and
598 C6+ improvements. Atmospheric Measurement Techniques **7**(12), 4353–
599 4365 (2014)

600 [15] Bhatt, R., Doelling, D.R., Angal, A., Xiong, X., Haney, C., Scarino, B.R.,
601 Wu, A., Gopalan, A.: Response versus scan-angle assessment of MODIS
602 reflective solar bands in Collection 6.1 calibration. IEEE Transactions on
603 Geoscience and Remote Sensing **58**(4), 2276–2289 (2020)

604 [16] Angal, A., Xiong, X., Wu, A., Geng, X., Chen, H.: Improvements in the
605 On-orbit response versus scan angle characterization of the Aqua MODIS
606 reflective solar bands. IEEE Transactions on Geoscience and Remote
607 Sensing **56**(3), 1728–1738 (2018)

608 [17] Bacour, C., Briottet, X., Bréon, F.-M., Viallefont-Robinet, F., Bouvet, M.:
609 Revisiting Pseudo Invariant Calibration Sites (PICS) over sand deserts
610 for vicarious calibration of optical imagers at 20 km and 100 km scales.
611 Remote Sensing **11**(10), 1166 (2019)

612 [18] IPCC: Climate change 2021: The physical science basis. contribution of
613 working group I to the sixth assessment report of the intergovernmen-
614 tal panel on climate change. In: Masson-Delmotte, V., Zhai, P., Pirani,
615 A., Connors, S.L., Péan, C., Berger, S., Caud, N., Chen, Y., Goldfarb,
616 L., Gomis, M.I., M. Huang, K.L., Lonnoy, E., Matthews, J.B.R., May-
617 cock, T.K., Waterfield, T., Yelekçi, O., Yu, R., Zhou, B. (eds.) Cambridge
618 University Press, Cambridge, UK and New York, NY, USA (2021)

619 [19] Ghimire, B., Williams, C.A., Masek, J., Gao, F., Wang, Z., Schaaf, C., He,

T.: Global albedo change and radiative cooling from anthropogenic land cover change, 1700 to 2005 based on MODIS, land use harmonization, radiative kernels, and reanalysis. Geophysical Research Letters **41**(24), 9087–9096 (2014)

[20] Smith, C.J., Kramer, R.J., Myhre, G., Alterskjær, K., Collins, W., Sima, A., Boucher, O., Dufresne, J.-L., Nabat, P., Michou, M., Yukimoto, S., Cole, J., Paynter, D., Shiogama, H., O'Connor, F.M., Robertson, E., Wiltshire, A., Andrews, T., Hannay, C., Miller, R., Nazarenko, L., Kirkevåg, A., Olivié, D., Fiedler, S., Lewinschal, A., Mackallah, C., Dix, M., Pincus, R., Forster, P.M.: Effective radiative forcing and adjustments in CMIP6 models. Atmospheric Chemistry and Physics **20**(16), 9591–9618 (2020)

[21] Lejeune, Q., Davin, E.L., Duveiller, G., Crezee, B., Meier, R., Cescatti, A., Seneviratne, S.I.: Biases in the albedo sensitivity to deforestation in CMIP5 models and their impacts on the associated historical radiative forcing. Earth System Dynamics **11**(4), 1209–1232 (2020)

[22] Hurtt, G.C., Chini, L.P., Frolking, S., Betts, R.A., Feddema, J., Fischer, G., Fisk, J.P., Hibbard, K., Houghton, R.A., Janetos, A., Jones, C.D., Kindermann, G., Kinoshita, T., Klein Goldewijk, K., Riahi, K., Shevliakova, E., Smith, S., Stehfest, E., Thomson, A., Thornton, P., van Vuuren, D.P., Wang, Y.P.: Harmonization of land-use scenarios for the period 1500–2100: 600 years of global gridded annual land-use transitions, wood harvest, and resulting secondary lands. Climatic Change **109**(1), 117 (2011)

[23] Feng, G., He, T., Wang, Z., Ghimire, B., Shuai, Y., Masek, J., Schaaf, C., Williams, C.: Multiscale climatological albedo look-up maps derived from moderate resolution imaging spectroradiometer BRDF/albedo products. Journal of Applied Remote Sensing **8**, 083532 (2014)

[24] Román, M.O., Schaaf, C.B., Lewis, P., Gao, F., Anderson, G.P., Privette, J.L., Strahler, A.H., Woodcock, C.E., Barnsley, M.: Assessing the coupling between surface albedo derived from MODIS and the fraction of diffuse skylight over spatially-characterized landscapes. Remote Sensing of Environment **114**(4), 738–760 (2010)

[25] Di Gregorio, A., Jansen, L.J.M.: A new concept for a land-cover classification system. The Land **2**, 55–65 (1998)

[26] Di Gregorio, A.: Land Cover Classification System: Classification Concepts and User Manual Softwave V2. Food and Agriculture Organization of the United Nations (FAO), Italy (2005)

[27] Friedl, M., Sulla-Menashe., D.: MODIS/Terra+Aqua Land Cover Type Yearly L3 Global 500m SIN Grid V061. figshare https://doi.org/10.5067/

MODIS/MCD12Q1.061 (2022)

[28] Sulla-Menashe, D., Gray, J.M., Abercrombie, S.P., Friedl, M.A.: Hierarchical mapping of annual global land cover 2001 to present: The modis collection 6 land cover product. Remote Sensing of Environment **222**, 183–194 (2019)

[29] Loveland, T.R., Belward, A.S.: The igbp-dis global 1km land cover data set, discover: First results. International Journal of Remote Sensing **18**(15), 3289–3295 (1997)